J Infrared Milli Terahz Waves (2016) 37:977–992
DOI 10.1007/s10762-016-0286-5

Transmission and Reflection Terahertz Spectroscopy of Insensitive Melt-Cast High-Explosive Materials

Norbert Palka[1] · **Mateusz Szala**[2]

Received: 16 February 2016 / Accepted: 3 May 2016 /
Published online: 30 May 2016

Abstract Currently, artillery shells and grenades that are introduced into the market are based on melt-castable insensitive high explosives (IHEs), which do not explode while they run a risk of impact, heat or shrapnel. Particles of explosives (such as hexogen, nitroguanidine and nitrotriazolone) are suspended in different proportions in a matrix of 2.4-dinitroanisole. In this paper, we investigated samples of commonly used IHEs: PAX-41, IMX-104 and IMX-101, whose internal structures were determined by a scanning electron microscope. Terahertz time domain spectroscopy was applied in both transmission and reflection configurations. At first, the complex refraction indices of four pure constituents creating IHEs were determined and became the basis of further calculations. Next, the experimentally determined transmission and reflection spectra of IHEs and pure constituents were compared with theoretical considerations. The influence of the grain size of constituent material and scattering on the reflection spectra was analysed, and good agreement between the experimental and theoretical data was achieved.

Keywords Time domain spectroscopy · Transmission · Reflectance · Insensitive high explosives

1 Introduction

Melt-castable explosive materials are used to manufacture artillery shells. Until now, pure explosives, e.g. 1,3,5-trinitro-1,3,5-triazacyclohexane (known as RDX), have been mixed with 2,4,6-trinitrotoluene (TNT) and melted by the application of heat. Then, they were poured into a shell, wherein they slowly cooled down to form an explosive charge. The shell-filling process is easy and comparatively cheap and has good performance. However, classical

✉ Norbert Palka
npalka@wat.edu.pl

[1] Institute of Optoelectronics, Military University of Technology, 00-908 Warsaw, Poland

[2] Faculty of Advanced Technologies and Chemistry, Military University of Technology, 00-908 Warsaw, Poland

materials manufactured on the basis of TNT may easily detonate because of impact with shrapnel, falling or temperature escalation. Bearing in mind numerous cases of accidental human victims over the last several years, mixtures based on TNT are replaced by insensitive high explosives with 2.4-dinitroanisole (DNAN) as the melting ingredient. Recently, the US Army introduced a family of melt-castable DNAN-based explosives containing mainly mixtures of RDX, 1-nitroguanidine (NQ) and 3-nitro-1,2,4-triazole-5-one (NTO) [1–4]. Trace amounts of *N*-methyl-*p*-nitroaniline (MNA) are included in some formulations to aid in the processing. IMX-101 (mixture of DNAN, NTO and NQ) replaces TNT as the main filler explosive in artillery projectiles. IMX-104 (mixture of DNAN, NTO and RDX) is qualified as a replacement for Composition B in mortars. PAX-41 containing DNAN and RDX is tested for spider grenades [1–4].

More and more growing threats caused by the use of explosive materials are forcing constant development of novel and modern methods for their detection [5]. One of the driving forces behind the development of the terahertz technique (the spectral range from 0.1 to 10 THz) is the fact that many commonly used explosive materials (such as RDX, PETN, HMX, TNT and NQ) have unique spectral features in this range of radiation [6–19]. Moreover, non-polar dielectric materials (such as clothes, paper and plastics) are relatively transparent in the range up to about 3 THz [6, 9], which raises hope of efficient identification of explosive materials remaining under cover or being inside packaging [6, 12]. Spectral examinations are mostly carried out by means of time domain spectroscopy (TDS) [6–11, 13, 17–19], Fourier spectrometry [10] and the use of a tunable source and broadband detector [12]. Most of the mentioned explosive materials have been thoroughly investigated in transmission [6–8, 13, 16] and in reflection configurations [7, 13]. Experiments have been carried out in different temperatures [14]; also, solid-state density functional theory calculations have been performed [15]. Methods for identifying explosive materials by means of their spectra are constantly being developed [16–19]. RDX is the most widely investigated material due to the fact that it is a constituent of many commonly used plastic materials (such as C-4 and Semtex) and melt-castable materials (like Composition B). RDX has a very clear absorption peak over relatively low frequencies—about 0.82 THz. This peak is crucial for its identification and is accompanied by a few other less clear peaks over higher frequencies [6–8, 10, 11, 13]. NQ has been quite well described in the literature as well—it has strong absorption peaks at 1.43, 2.38 and 2.76 THz [6]. In contrast, DNAN has only been briefly characterized [20]. Terahertz investigations of NTO and IHEs were not found at all in the literature.

First, it should be noted that sample preparation is a very important factor in obtaining reliable spectra in the terahertz range. The commonly used transmission configuration [6–8, 13, 16] gives clearly visible absorption peaks that may later be used as the basis for the identification of explosive materials. With regard to quite big attenuation (~100–300 cm^{-1}) [6], practical applications are limited to rare situations such as measurements of the thin layer of the powder placed in the envelope. For this reason, all samples prepared to transmission measurements are in the form of pressed pellets consisting of material with good transmission in the terahertz range (such as polyethylene) with suspended explosive material particles with a concentration of 5–20 %, which allows for proper determination of absorption characteristics [6] but ensures sufficient transparency. In real applications, only reflection configuration can be applied because terahertz radiation cannot transmit through targets thicker than a few millimetres. Samples for reflection measurements are mostly manufactured in the form of pressed pellets but consisting of pure explosive material powder, sometimes with a few per cent addition of desynthesizer [7]. The interaction of the terahertz wave with the surface of the

sample depends on its morphology. Specular reflection takes place when the sample has a flat and smooth surface. If the particle size of the solid material is comparable to the terahertz wavelength, the scattering may cause a significant change in the obtained spectrum [21]. First, we manufactured pressed pellets of considered explosive materials. To approach the most realistic conditions, we also prepared melt-castable samples, where the solubility of materials in DNAN and grain sizes of particles were analysed.

Here, we investigated three prospective IHEs, PAX-41, IMX-104 and IMX-101, by means of a terahertz TDS system both in transmission and reflection configurations. Samples were prepared as pressed pellets and melt-castable discs. Their surface morphology and grain sizes were determined by means of a scanning electron microscope (SEM). For terahertz measurements, the TDS method was used due to its sensitivity and high measurement dynamics. First, the complex transmission characteristics of four materials (RDX, NQ, NTO and DNAN) were determined to provide the exact data for further calculations. Next, the transmission characteristics of pellets manufactured from IHEs and the reflection characteristics of pellets from pure materials and discs made from IHEs were measured. The results of IHE measurements, both in transmission and reflection configurations, maintain good agreement with theoretical calculations. Images from SEM investigations help to draw conclusions about the phenomena taking place during the reflection.

2 Sample Preparation and Characterization

Although the literature concerning IHEs is quite impressive, the details of their manufacturing process are not available due to the sensitive character of such data and patent claims. Because of this, samples were prepared based on the literature [1–3] as well as on our experience. Three types of samples were prepared: pressed pellets for transmission (denoted by the suffix p) and reflection (denoted by the suffix P) measurements and melt-castable discs (denoted by the suffix C) for reflection measurements (Table 1, Fig. 1).

For transmission configuration, the explosive materials were ground using a mortar and pestle to reduce the particle size below 50 μm, which suppresses scattering losses [6, 20]. Due to the high attenuation of pure explosives, we mixed them with fine polyethylene (PE) powder (used as a matrix), which is highly transparent in the terahertz range [6]. The mixing ratio was 5 % weight of a material to total weight of mixed samples. Afterwards, the resultant fine powder was pressed into a pellet directly using a hydraulic press. As a result, we obtained the 13-mm-diameter pellets listed in Table 1 (numbers 2–8), which consisted of 20 mg of explosive material and 360 mg of PE (Fig. 1a). As a reference, a 360-mg pellet pressed from pure polyethylene was prepared (number 1). Although the powders were thoroughly mixed, the low concentration of the constituent materials in the sample (e.g. 1.25 % RDX in IMX-104) can result in fluctuations in their distribution, which may later lead to disturbances of the obtained terahertz spectra. For reflection investigation, fine powders of pure explosives and IHE materials (numbers 9–15) were pressed into pellets with a weight of about 5 g, thickness of 5 mm and diameter of 30 mm (Fig. 1b). Macroscopically, surfaces of the samples were flat and smooth. However, SEM investigations (by Quanta 3D FEG) revealed that the surfaces were slightly rough and consisted of grains of crystals with dimensions below 100 μm and flat surfaces (Fig. 2a–c). In all reflection measurements, a gold mirror was used as a reference.

The melt-castable samples were prepared as 30–40-mm-diameter discs with one flat and smooth surface, which suppresses surface-dependent scatterings and allows the interaction of

Table 1 Samples prepared for measurements

	Type	Name	Ingredients	Composition [%]	Particle size [μm][a]	Form
1	Transmission	PE	PE	100	<50	13-mm pellet
2		RDX_p	PE/RDX	95/5	<50	13-mm pellet
3		NQ_p	PE/NQ	95/5	<50	13-mm pellet
4		NTO_p	PE/NTO	95/5	<50	13-mm pellet
5		DNAN_p	PE/DNAN	95/5	<50	13-mm pellet
6		PAX-41_p	PE/DNAN/RDX	95/0.05x (60/40)	<50	13-mm pellet
7		IMX-104_p	PE/DNAN/NTO/RDX	95/0.05x (35/40/25)	<50	13-mm pellet
8		IMX-101_p	PE/DNAN/NTO/NQ	95/0.05x (44/20/36)	<50	13-mm pellet
9	Reflection	RDX_P	RDX	100	<100	30-mm pellet
10		NQ_P	NQ	100	<100	30-mm pellet
11		NTO_P	NTO	100	<100	30-mm pellet
12		DNAN_P	DNAN	100	<50	30-mm pellet
13		PAX-41_P	DNAN/RDX	60/40	<50/<100	30-mm pellet
14		IMX-104_P	DNAN/NTO/RDX	35/40/25	<50/<150/<150	30-mm pellet
15		IMX-101_P	DNAN/NTO/NQ	44/20/36	50/150/150	30-mm pellet
16		D90R10	DNAN/RDX	90/10	<50/<100	Cast
17		PAX-41_100	DNAN/RDX	60/40	<50/<100	Cast
18		PAX-41_200	DNAN/RDX	60/40	<50/200–250	Cast
19		PAX-41_300	DNAN/RDX	60/40	<50/300–350	Cast
20		IMX-104_C	DNAN/NTO/RDX	35/40/25	<50/<150/<150	Cast
21		IMX-101_C	DNAN/NTO/NQ	44/20/36	<50/<150/<150	Cast

[a] Before melting

the radiation with the material to be focused upon (Fig. 1c). The powders of RDX, NQ and NTO (synthesized at the Military University of Technology according to the original procedures) were sieved by using a vibratory sieve shaker AS 200 control (Retsch), in order to obtain the desired grain diameters. Cast samples were prepared by using laboratory-scale melt-pour apparatus equipped with a thermocycler and heated pot. DNAN was heated in the pot to a temperature of 110 °C until it was totally melted. Next, a mechanical stirrer was started up and solid ingredients were added in small portions. The mixture was stirred for 15 min until the composition was homogenous. The casting was realized by tilting the melting pot, and the composition was poured into a rubber mould placed on glass. After solidification, the cast disc was recovered and tested using the methods described below. The mixture of DNAN and RDX was studied more deeply to enable understanding of solubility-related phenomena. Since the solubility of RDX in DNAN is about 10 % (at 100 °C), we manufactured the D90R10 sample (number 16), which consisted of 90 % of DNAN and 10 % of RDX. Next, we prepared three samples with various mean grain sizes of RDX particles (below 100, 200–250 and 300–350 μm) to study the influence of solubility and scattering. They are called PAX-41_100, PAX-41_200 and PAX-41_300, respectively (numbers 17–19). The sample of IMX-104 (IMX-101) consisted of mixed powders of RDX and NTO (NQ and NTO) with a particle

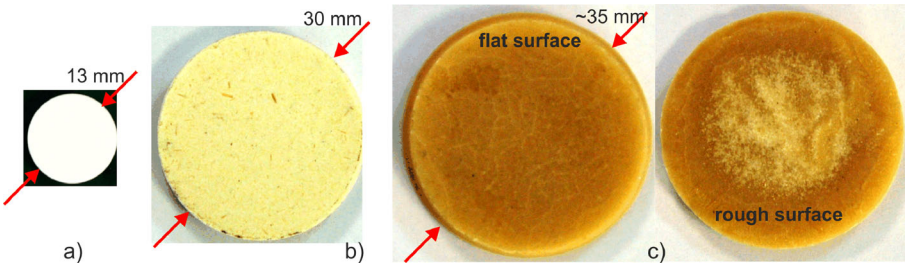

Fig. 1 Photographs of the samples: 13-mm pellet for transmission (**a**), 30-mm pellet for reflection (**b**), and melt-castable disc for reflection (**c**)

grain size below 150 μm (numbers 20–21). The solubility of NQ and NTO in DNAN is about 1 % at 100 °C.

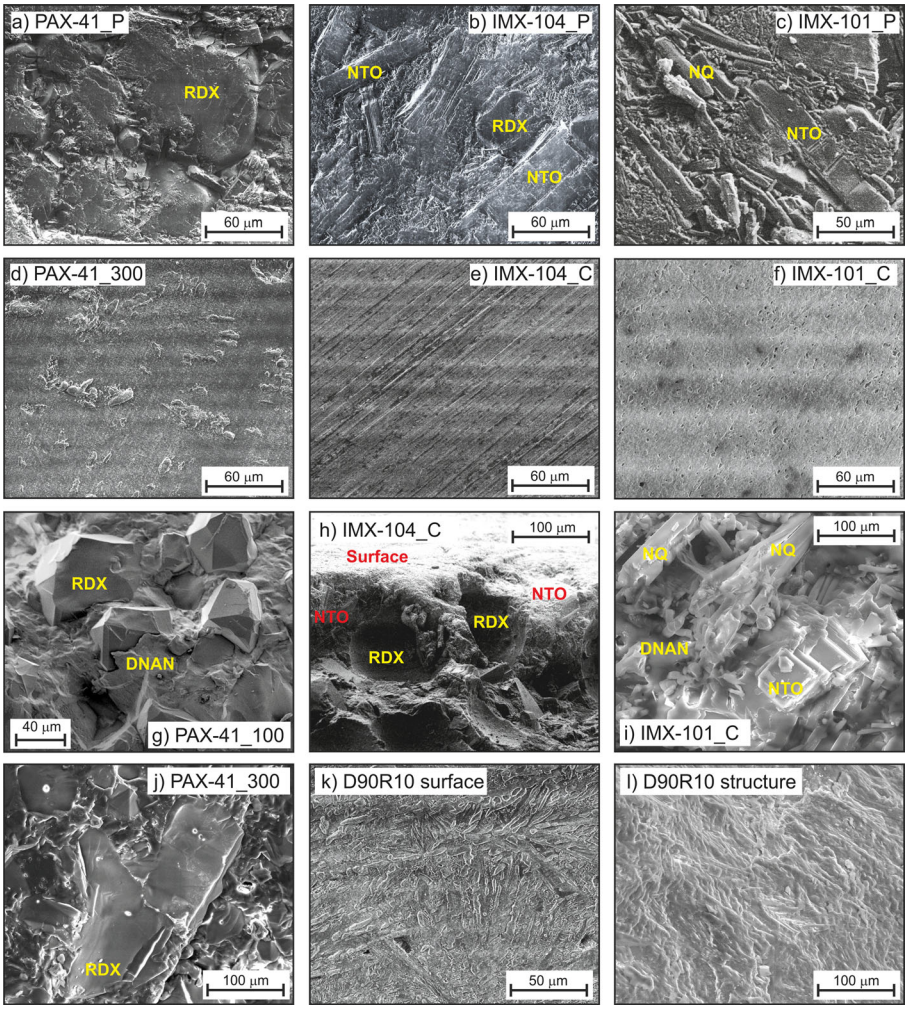

Fig. 2 SEM images of the surfaces of the samples and of their internal structures

Both the internal structure of the cast disc (revealed from small broken-off pieces) and its surface were imaged using an SEM microscope. The surfaces of the manufactured samples were flat and macroscopically smooth (Fig. 2d–f, k) due to the fact that smooth and flat glass was used in pouring compositions into rubber moulds. Small scratches, holes and micro-cracks that were caused by the solidification process had dimensions up to 10 μm and are not significant from the point of view of terahertz radiation.

The D90R10 sample should consist of totally molten RDX. But during cooling down, a part of RDX is recrystallized to the form of crystalline grains smaller than 20 μm. The exact efficiency of recrystallization and the size of those grains are not known to the authors. Assuming that 50 % of RDX will transform into a crystalline form, the D90R10 sample will consist of 95 % of solid solution of RDX in DNAN and 5 % of small grains. Figure 2l shows the homogenous structure of the D90R10 sample. In samples from the PAX-41 group, small RDX crystals are totally dissolved while bigger crystals have a reduced size. After cooling down and recrystallization, the samples consist of around 63 % of solid solution of RDX in DNAN and also of small grains of RDX and partially melted original grains. For the PAX-41_100 sample, the characteristic polyhedral RDX crystals (with dimensions of 10–80 μm) are clearly seen (Fig. 2g). For the PAX-41_300 sample (Fig. 2j), a large central crystallite (around 250 μm) is shown together with a number of smaller crystallites with sizes of 20–100 μm.

The IMX-101_C sample consists of around 37 % of solid solution of RDX in DNAN, less than 20 % of RDX crystals of different sizes, but all smaller than 150 μm, and around 40 % of oblong cuboid NTO crystals of diverse sizes up to 150 μm. Figure 2h shows a cross section of the sample, where the surface of the sample can be clearly seen and cuboid NTO crystallites located on the surface are visible together with holes after RDX crystallites. The IMX-101_C sample consists of dominant needle-shaped grains of NQ and cuboid NTO crystallites suspended in a solid solution of DNAN (Fig. 2i). The sizes of the NQ and NTO crystals are below 150 μm.

3 Experimental and Data Analysis

In the range of terahertz radiation, time domain spectroscopy is the most commonly applied method and has already been thoroughly described [6–11, 13, 17–19]. Here, we carried out an experiment using a TPS 3000 (TeraView) spectrometer, which is a commercially available TDS set-up ready to operate in transmission and reflection configurations. In transmission, the pellets were located in the focus of the optical system. The reflection set-up had an incident angle of $\alpha = 22°$ (Fig. 3) and was an extension of the transmission arrangement created by adding flat and off-axis parabolic mirrors with 50-mm focal lengths. In reflection, the sample was located on a stage and moved manually in X-Y directions to measure 20 different points on the sample. The surface of all samples and the gold mirror were positioned exactly in the focus of the optical system with an error of about 10 μm, which was controlled by the micrometer screw (in the Z direction). This condition is crucial for appropriate determination of the reflection spectrum; however, a misplacement phase error correction was also developed [22]. In the transmission (reflection) set-up, we also determined beam diameters using the knife-edge method [23]; these are equal to about 1.9, 0.9 and 0.5 mm (1, 0.7 and 0.4 mm) at frequencies of 0.5, 1 and 2 THz, respectively.

The TDS system used a pulse lasting about 0.4 ps (which is full width at half-maximum value). This signal has a 0.1–3-THz useful spectral range (Fig. 3). Each 40-ps-long waveform

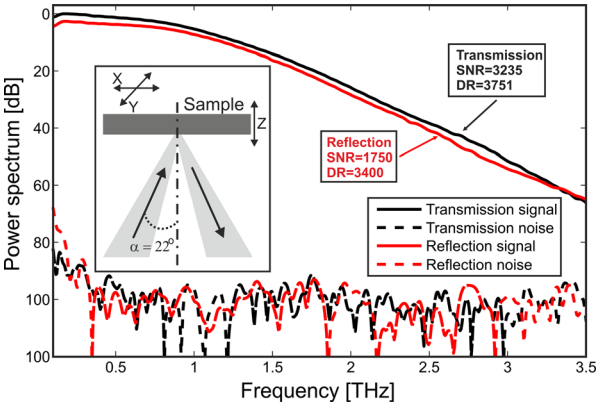

Fig. 3 The power spectrum of the pulses and the noise levels in transmission and reflection configurations. *SNR* and *DR* denote the signal-to-noise ratio and the dynamic range, respectively. The *inset* shows a schematic diagram of the reflection configuration

was measured with a resolution of 2048 points and averaged 3000 times. Then, Blackman-Harris third-order filtering was applied to apodize the time signal, which smoothed the spectrum. Therefore, 3 min was enough for a single measurement. In Fig. 3, the power spectrum of the pulses and the noise levels are shown for transmission and reflection configurations. Such spectra are available when the influence of water vapour is minimized by purging the chamber with dry air. To assess system performance, the signal-to-noise ratio and dynamic range were determined in the frequency domain according to the algorithm presented in [24] (Fig. 3).

The main advantage of the transmission TDS technique is that one can easily determine the complex refractive index ($N=n+i\cdot\kappa$) of a measured material [6]. The power absorption coefficient (α) can be calculated as

$$\alpha = \frac{4\pi\nu\kappa}{c} \tag{1}$$

where c is the speed of light, ν is the frequency and κ is the extinction coefficient. The presented method requires precise determination of the thicknesses of the reference (PE) and the sample (with explosive) pellets.

Assuming that the s-polarized beam incidents from the air on the sample, its complex amplitude reflection coefficient ($\tilde{r}$) can be calculated from the Fresnel formula as

$$\tilde{r} = r\cdot\exp(\Delta\varphi) = \frac{\cos\alpha - N\sqrt{1-\left({}^{1}/_{N}\sin\alpha\right)^{2}}}{\cos\alpha + N\sqrt{1-\left({}^{1}/_{N}\sin\alpha\right)^{2}}} \tag{2}$$

where r is the amplitude reflection coefficient and $\Delta\phi$ is the reflectance phase. The reflectance R is related to the amplitude reflection coefficient by $R=r^2$. The reflectance spectrum (R) mimics the refractive index (n) variations, while the reflectance phase ($\Delta\phi$) represents the absorption features similarly to the extinction coefficient (κ) in transmission [7].

For unary pellets with small-size particles (samples 9–12), we used the N index directly taken from transmission measurements (Fig. 4). The interaction between the terahertz waves and the multi-component samples (26–27), which are a dielectric mixture, can be quantitatively described using the effective medium theory (EMT) [25, 26]. Although EMT assumes that the particle size is much smaller than the wavelength of the electromagnetic radiation, we proved that the experimental results are also consistent with the theory for the particles equal to

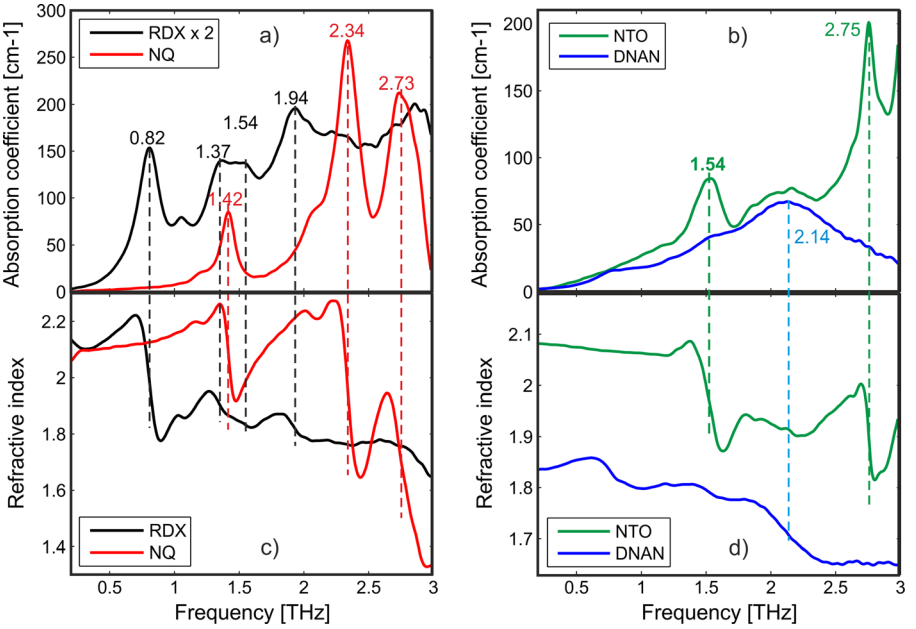

Fig. 4 The absorption coefficients and the refractive indices of the RDX_p and NQ_p (**a**, **c**) and NTO_p and DNAN_p (**b**, **d**) samples

or slightly smaller than the wavelength. EMT considers that the wave is averaged over the volume of the sample and experiences an effective refractive index N_{eff}. Due to the variety of sizes, shapes and orientations of RDX, NTO and NQ particles diluted in the DNAN (which is a uniform matrix), we calculated N_{eff} as the average refractive index of the constituent materials (Figs. 5, 6, 7, 8 and 9), taking into account their volumetric composition. The correlation coefficient (C) was used as a parameter, which quantitatively describes the agreement between experimental and theoretical data and is included in Figs. 5, 6, 7, 8, 9 and 10.

4 Transmission Results and Discussion

Complex spectra of the RDX_p, NQ_p, NTO_p and DNAN_p samples (Fig. 4) reveal the absorption peaks which are connected with slopes of the refractive index characteristics. In the case of RDX and NQ, the positions of peaks agree well with the literature [6–8, 10, 11, 13]. Some discrepancies can be attributed to the different manufacturer of materials and fluctuations in their density inside the sample. NTO shows two distinctive absorption peaks at 1.54 and 2.75 THz, while DNAN has a broad and flat peak at 2.14 THz.

Figure 5 plots the spectra of the PAX-41_p, IMX-104_p and IMX-101_p samples directly measured in the TDS set-up and calculated based on the spectra of their constituents (Fig. 4) and their concentration (Table 1). The good agreement between the measurement and the calculation proved that the features appearing in the absorption and the refractive index characteristics can be understood from the sum of the constituents. Slightly shifted features of RDX (at 0.82 and 1.58 THz) and DNAN (at 2.2 THz) are observed for PAX-41, because it consisted of approximately equal amounts of constituent materials. In the case of IMX-104, the

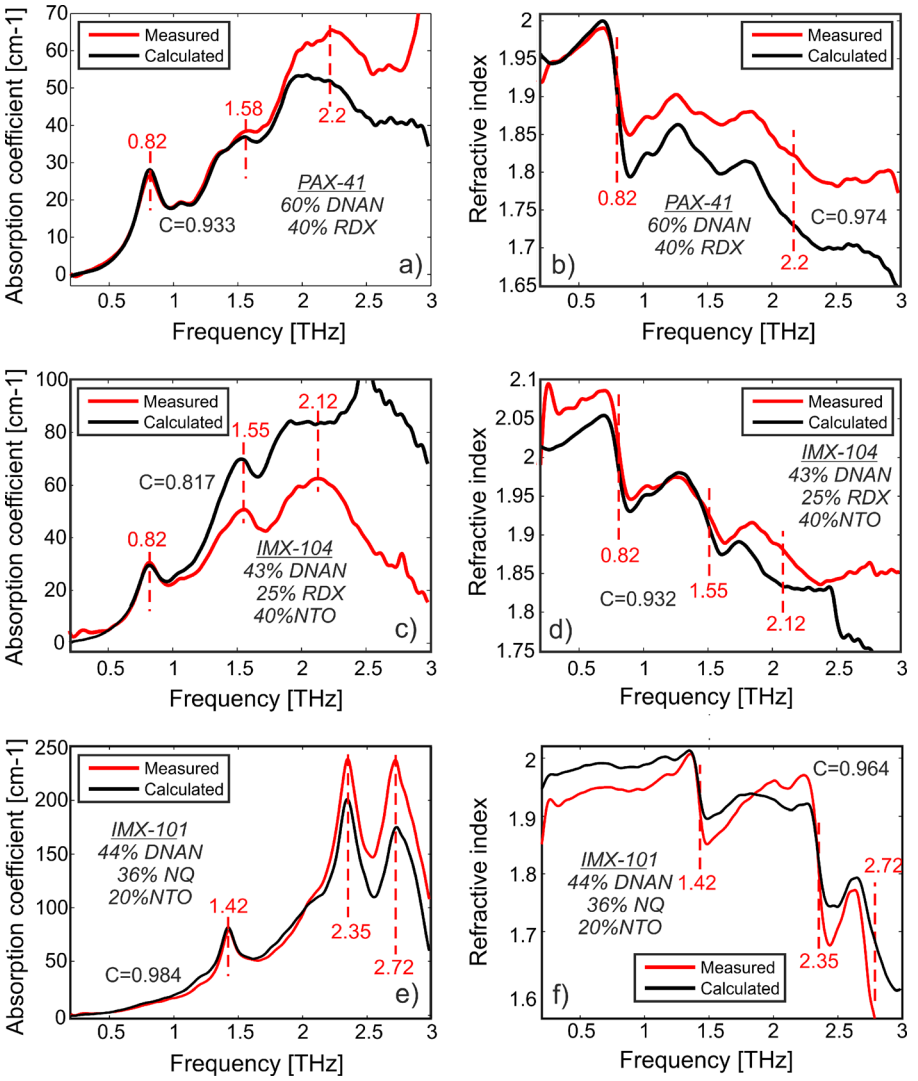

Fig. 5 The absorption coefficients and refractive indices (measured and calculated from constituents) of PAX-41 (**a**, **b**), IMX-104 (**c**, **d**) and IMX-101 (**e**, **f**)

feature at 0.82 THz can be attributed to RDX, the one at 1.55 THz to RDX or NTO and the one at 2.12 THz to DNAN. For IMX-101, high NQ peaks dominate over DNAN and NTO. Some observed discrepancies were due to the local fluctuations in the concentration and thickness of material both in the case of samples with pure explosives (Fig. 4) and IHEs (Fig. 5).

5 Reflection Results and Discussion

Figure 6 shows the complex reflection spectra (the reflectance R and the phase $\Delta\phi$) of 30-mm-diameter pellets: RDX_P, NQ_P, NTO_P and DNAN_P. The spectra were directly measured in

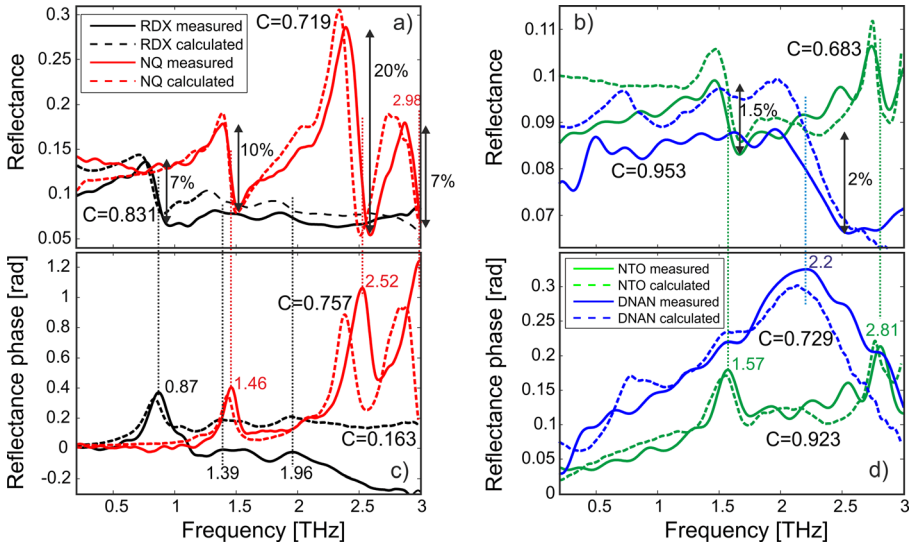

Fig. 6 The reflectance spectra of the NQ_P and RDX_P (**a**, **c**) and NTO_P and DNAN_P (**b**, **d**) samples

the TDS set-up and calculated for comparison based on Eq. 2 and the measured absorption spectra (Fig. 4). As expected, the reflectance characteristic mimics the refractive index variations, while the reflectance phase is similar to the absorption characteristic. The RDX characteristic has an amplitude decrease (slope) of about 7 % centred at 0.87 THz. For NQ, we can see three distinctive features in the reflectance phase at 1.46, 2.52 and 2.98 THz that correspond to the amplitude slopes of 10, 20 and 7 % in the reflectance characteristic, respectively. The NTO spectrum contains a feature whose amplitude slope is about 1.5 % at 1.5 THz, while DNAN has a 2 % decrease centred at 2.2 THz.

The measured reflectance and phase characteristics are shifted towards higher frequencies in comparison with the calculated spectra. The phase spectrum of RDX (Fig. 6c) has a

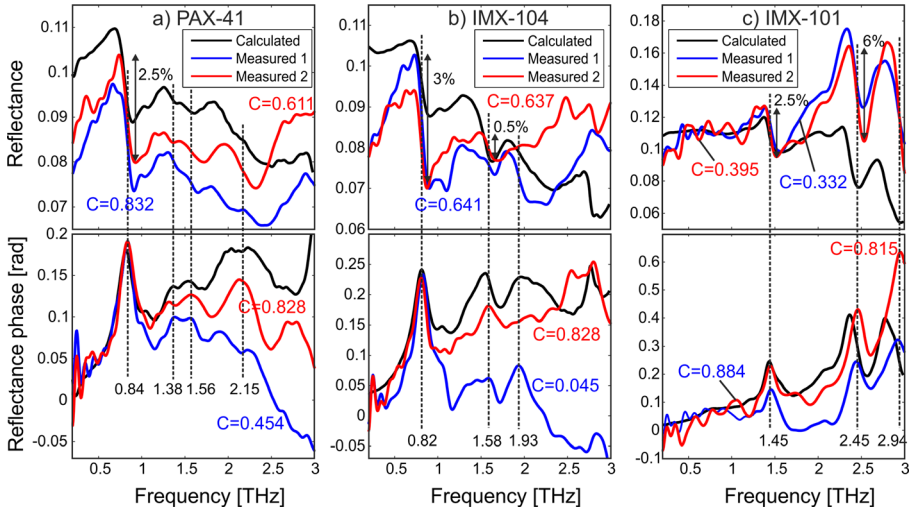

Fig. 7 The reflectance spectra of 30-mm pellets: PAX-41_P (**a**), IMX-104_P (**b**) and IMX-101_P (**c**)

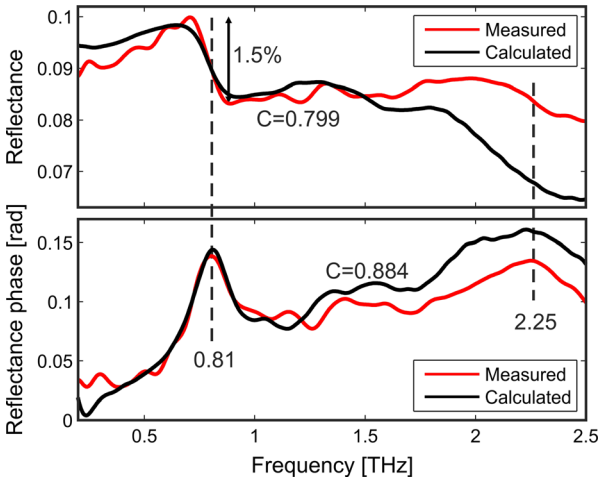

Fig. 8 The reflection spectrum of the D90R10 sample

declining character, due to the slightly different position of the sample and the mirror surfaces (misalignment error).

The reflectance of the 30-mm-diameter pellets of IHE samples (numbers 13–15) depended on the point of measurement on the sample. Figure 7 presents only the best characteristics obtained for each sample. The number of points with the appropriate spectrum was equal to about 90, 40 and 50 % for PAX_41_P, IMX-104_P and IMX-101_P, respectively. For PAX-41_P (Fig. 7a), the RDX features at 0.82, 1.38 and 1.56 THz are clearly visible for two different measurement points. Scattering of the terahertz beam at the RDX particles is noticeable at higher frequencies, and the feature of DNAN at 2.15 THz is ambiguous. Probably, due to local fluctuation of constituent distribution, in the case of the IMX-104_P

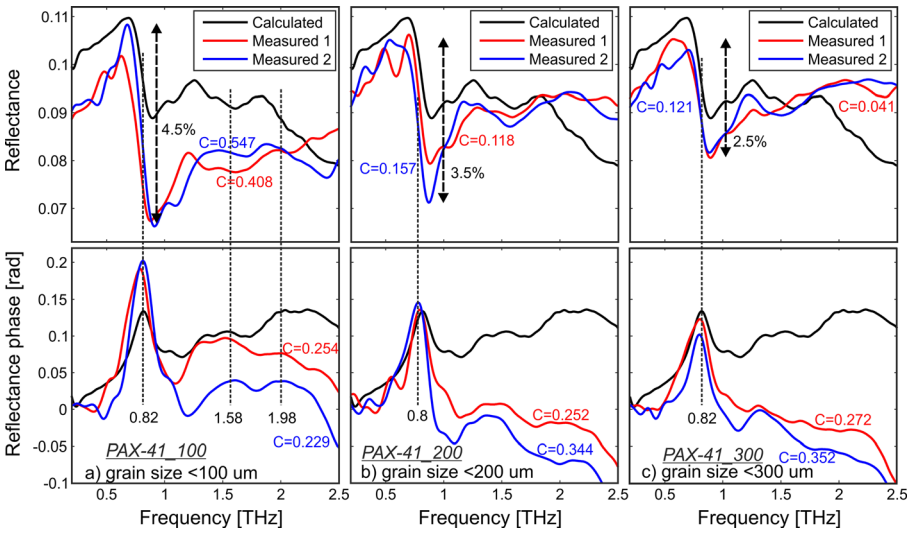

Fig. 9 The reflection spectra of PAX-41—calculated and measured at two points for samples with three grain sizes (100, 200 and 300 μm diameter)

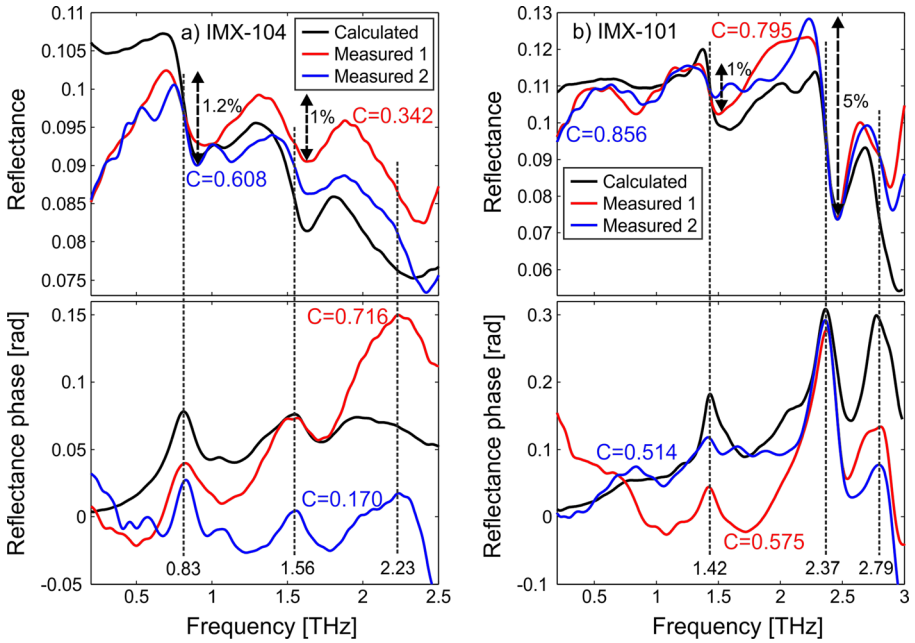

Fig. 10 The reflection spectra of IMX-104_C (**a**) and IMX-104_C (**b**)—calculated and measured at two points

sample, which had a lower concentration of RDX (25 %) in comparison to PAX-41_P (40 %), the feature of RDX at 0.82 THz has a higher reflectance slope with an amplitude equal to about 3 % (Fig. 7b) in comparison to PAX-41_P (2.5 %). The features of NTO at 1.58 THz and RDX at 1.93 THz are not always present. Three NQ-related features in the reflectance spectrum of IMX-101_P are clearly visible at 1.45, 2.45 and 2.94 THz (Fig. 7c). The calculated spectra (black curves) agree well with the experiment up to about 1.5–2 THz. At higher frequencies, both the local fluctuation in constituent distribution and the scattering modified the experimental characteristics.

The exemplary reflection spectrum of the melt-castable D90R10 sample (Fig. 8) revealed a 1.5 % RDX-origin slope in reflectance at 0.81 THz conjugated with the peak of the reflectance phase ($\Delta\phi$). The feature at 2.25 THz can be attributed to both DNAN and RDX. A similar result could be obtained at almost every point of the sample, because it was uniform, since RDX was totally dissolved in DNAN. The proposed effective medium theory is consistent with the experiment. Since this sample consisted of 95 % of homogenous solid solution of RDX in DNAN and 5 % of small (below 10 μm) recrystallized RDX grains, its surface and volume (Fig. 2k, l) were uniform for the terahertz radiation with a beam diameter of about 0.5–1 mm and wavelength in the range 100–1000 μm. Some discrepancies at higher frequencies are probably the result of the scattering phenomenon.

Surfaces of the cast samples from the PAX-41 family with different grain sizes (100, 200 and 300 μm) were smooth and uniform. They consisted mainly of the homogenous solid solution of RDX in DNAN (Fig. 2d). However, the reflectance depended on the measurement point on the sample—in some of them, the RDX features at 0.82 THz (both the slope in the reflection curve and the peak in the phase characteristic) were deformed and in a few of them not visible at all (Fig. 9). Although the concentration of the RDX in DNAN was constant and

equal to 40 %, the number of points without the appropriate spectrum were equal to about 10 % for PAX-41_100 and 20 % for both PAX-41_200 and PAX-41_300.

For PAX_100, smaller particles of RDX were probably more uniformly packed in the sample and the scattering was also lower. Figure 9 presents reflectance curves of the PAX-41 family measured at two selected points with the highest slope of RDX at 0.82 THz. For 100 and 200 μm grain sizes (Fig. 10a, b), the amplitude of the RDX slope at 0.82 THz is two times bigger than the EMT-based calculations, which may be attributed to the local concentration of RDX grains. For PAX-41_300 with higher grain size, the scattering increased, which resulted in a smaller amplitude of the slope at 0.82 THz, while the average reflectance remained constant and equal to about 0.09 (Fig. 9). The feature of DNAN at about 2.1–2.2 THz is not visible. At higher frequencies, the scattering suppresses the expected features for all cases.

The surface of the melt-castable disc, as in the PAX-41 case, was smooth and uniform and consisted mainly of the solid solution of RDX in DNAN (Fig. 2e). Moreover, the cross section of the IMX-104_C (Fig. 2h) presents a solid solution of RDX in DNAN and less than 150-μm-size particles of RDX (polyhedral) and NTO (rectangular). Since the IMX-104_C sample consists of 40 % of NTO and 25 % of RDX, the feature of RDX at 0.82 THz has a smaller reflectance slope than PAX-41 with an amplitude equal to about 1.2 %. However, features of NTO at 1.56 THz and DNAN at about 2.23 THz can be seen (Fig. 10a). Although the visibility of the features is rather small, the number of points with the appropriate spectrum is equal to about 90 %. The calculated spectrum agrees well with the experiment, but the amplitude of the RDX slope at 0.82 THz is smaller than expected, while the NTO-related amplitude at 1.56 THz is bigger, which probably resulted from fluctuation in the concentration of constituent grains.

As expected, the reflection spectrum of the IMX-101_C sample is dominated by NQ features, which are visible at 1.42, 2.37 and 2.79 THz (Fig. 10b). Due to the high scattering at higher frequencies, the feature at 2.79 THz is not always present. However, the melting process broke up some of the larger needle-shape NQ grains into smaller ones (Fig. 2i) and we think that the surface layer of the sample consisted mainly of a mixture of melted DNAN with fine NQ grains, which justifies the very good visibility of the NQ features even at higher frequencies. At 1.42 and 2.37 THz, the reflectance slope has an amplitude equal to about 1 and 5 %, respectively. The features of NTO at 1.54 THz and DNAN at about 2.1 THz are not visible. Probably due to clustering of the NQ grains, the number of points with an appropriate spectrum is about 40 %. The EMT-based calculated spectrum is in line with the experiment.

6 Summary and Conclusions

The examination of explosive materials by means of terahertz transmission and reflection spectroscopy is very promising. In the transmission configuration, the absorption peaks are connected with the slopes of the refractive index (Fig. 4) as was proven for two well-known and popular explosives (RDX and NQ) and two materials seldom investigated in the terahertz domain (NTO and DNAN). Two unique absorption peaks at 1.54 and 2.75 THz can be observed for NTO, while DNAN is characterized only by one flat and relatively broad peak at 2.14 THz. Next, the transmission spectra of all IHEs were calculated with the use of characteristics of constituent materials and remained in good agreement with experimental measurements. This means that all peaks observed in the absorption characteristics have their corresponding slope on the refractive index curve, and moreover, all these features are directly

connected with features of all constituents (Fig. 5). Of course, by comparing pure explosive materials and IHEs, some discrepancies can be distinguished and it is presumed that they result from local fluctuations in the concentration and thickness of materials.

The second method of terahertz examination of IHEs referred to the reflection spectra measurements. As before, we determined the characteristics of pure explosive materials (Fig. 6), but in comparison with the calculated spectra, their reflectance curves and phase characteristics were shifted towards higher frequencies. Summarizing, we can see that the reflectance characteristic corresponds to the refractive index variations and the reflectance phase to the absorption characteristic. Here, even a small misalignment of the sample surface or the reference mirror could cause some deviations from proper characteristics. The acceptable misalignment error is 10 μm.

Finally, the reflectance characteristics of IHE pellets were compared to the EMT-based calculations (Fig. 7). We think that the main role in the reflection measurements plays the surface-related scattering and not uniform surface distribution of the grains (Fig. 2a–c), which led to the proper reflectance characteristics being observed not at all measuring points. The surfaces of the IHE melt-castable discs were flat and uniform, and the terahertz radiation interacted with grains of RDX, NTO and NQ buried in the surface layer of the sample. In the case of RDX-based materials (PAX-41 and IMX-104), the solid solution of RDX in DNAN created the matrix, which enabled easier interaction with the particles. In the case of discs, we should also consider melt-related phenomena such as local concentration of the particles, clustering, breaking up of the particles and scattering at higher frequencies. The proposed effective medium theory offers a simple yet qualitatively correct description of the reflection from the complicated granular media. Better understanding of the related phenomena also requires consideration of the influence of the size of the terahertz beam. For 0.8 THz (RDX peak), the 1/e beam diameter is about 2 mm, while for 2.5 THz (NQ peak), it is below 0.5 mm. This factor can also explain the lower hit ratio of PAX-101 than for RDX-based IHEs.

The correlation coefficient between the measured and the theoretically calculated spectra has very high value for the transmission configuration. In all transmission cases, C is larger than 0.8 (Fig. 5) which is the sufficient confirmation of adequate choosing the EMT analysis method. For reflection measurements in most of the considered cases, the value of the correlation coefficient is high, but there are also some cases when it drops to small values (like for example in Figs. 6c and 7c), which results from the fact that the range 0.1–3 THz was used for correlation calculations. However, for both these cases, the similarity of the spectra is clearly seen, as well as the location of absorption peaks. For frequencies higher than 2 THz, often there are significant distortions of the spectrum which introduce a lower correlation value. Moreover, limiting the spectral range to 2 THz would mean that some distinctive spectral features would not be taken into account, which additionally depreciates the reliability of performed calculations. To compare such spectra, a more intelligent method as the principle component analysis can be used.

To sum up, we presented a comprehensive analysis of three melt-castable explosive materials and their constituents both in transmission and reflection. We proved that based on the refraction index of four constituent materials (DNAN, RDX, NTO and NQ) and EMT, we can calculate the reflection spectra of the IHEs with good agreement. In reflection, thanks to SEM images of the samples (pressed pellets and melt-castable discs), we explained the modifications of their reflectivity. In our opinion, grain-related scattering and clustering of particles must be considered. The presented analysis reveals that terahertz spectroscopy can be applied for reflection identification of IHEs. However, due to the inhomogeneity of the

samples, measurement at a few (or even at a dozen) points must be considered to obtain reliable results. Moreover, since IHE materials are insensitive to compression, one can also measure their spectra by using an attenuated total reflection technique [27], in which sample preparation is easier than with pressed pellets.

In the future, the terahertz radiation can be used as a safe, fast and non-destructive method for quality control and examination of explosives. This radiation is absolutely non-ionizing and there is no risk of accidental initiation of the explosive being under tests. The results obtained by using the TDS method without doubt encourage further development of terahertz examination techniques and applying them to non-destructive analysis of explosives having a similar qualitative composition as the materials described in this paper. Moreover, this method allows for the detection of explosives containing relative compounds. Thus, the next step is to move from DNAN evaluation to analysis of trinitroanisole (TNAN), which can also be used as the melting ingredient.

Acknowledgments The paper was supported by the Military University of Technology under projects PBS-830 and PBS-906.

References

1. U.R. Nair, S. N. Asthana, A. Subhananda Rao, B.R. Gandhe, Defence Sci. J. 60, 137 (2010).
2. K. Dontsova, S. Taylor, R. Pesce-Rodriguez, M. Brusseau, J. Arthur, N. Mark, M. Walsh, J. Lever, and J. Simunek, IHE Dissolution of NTO, DNAN, and Insensitive Munitions Formulations and Their Fates in Soils, http://acwc.sdp.sirsi.net/client/search/asset/1036642 IHE. Accessed 15.01.2016.
3. P. J. Davies, A. Provatas, Characterisation of 2,4-Dinitroanisole: An Ingredient for use in Low Sensitivity Melt Cast Formulations, www.dtic.mil/cgi-bin/GetTRDoc?AD=ADA458880, Accessed 15.01.2016.
4. W. A. Trzcinski, S. Cudzilo, S. Dyjak, M. Nita, Central European Journal of Energetic Materials 11, 3 (2014).
5. J. Wojtas, T. Stacewicz, Z. Bielecki, B. Rutecka, R. Medrzycki, J. Mikolajczyk, Opto-electron. Rev. 21, 9 2013.
6. J. Chen, Y. Chen, H. Zhao, G. Bastiaans, X.-C. Zhang, Opt. Express 15, 12060 (2007).
7. K. Choi, T. Hong, K. Sim, T. Ha, B. C. Park, J. H. Chung, S. G. Cho, J. H. Kim, J. Appl. Phys. 115, 2 (2014).
8. A. K. Huhn, E. Sáenz, IEEE Trans. THz Sci. Technol. 3, 5 (2013).
9. E. Hérault, F. Garet, IEEE Trans. THz Sci. Technol. Accepted for publication.
10. Y. C. Shen, T. Lo, P. F. Taday, B. E. Cole, W. R. Tribe, M. C. Kemp, Appl. Phys. Lett. 86, 241116 (2005).
11. M. R. Leahy-Hoppa, M. J. Fitch, X. Zheng, L.M. Hayden, R. Osiander, Chem. Phys. Lett. 434, 4-6 (2007).
12. K. Kawase, Y. Ogawa, H. Minamide, H. Ito, Semicond. Sci. Technol. 20, S258 (2005)
13. H. Zhong, C. Zhang, L. Zhang, Y. Zhao, X-Ch. Zhang, Appl. Phys. Lett. 92, 221106 (2008).
14. J. Barber, D. E. Hooks, D. J Funk, R. D Averitt, A. J. Taylor, D. Babikov, J. Phys. Chem. A. 109, 15 (2005).
15. L. Huang, A. Shabaev, S. G. Lambrakos, N. Bernstein, V. Jacobs, D. Finkenstadt, L. Massa, J. Mater. Eng. Perform. 21, 7 (2011).
16. F. Ellrich, G. Torosyan, S. Wohnsiedler, S. Bachtler, A. Hachimi, J. Jonuscheit, R. Beigang, F. Platte, K. Nalpantidis, T. Sprenger, D. Hübsch, "Chemometric Tools for Analyzing Terahertz Fingerprints in a Postscanner," 37th International Conference on Infrared, Millimeter and Terahertz Waves (2012).
17. A. D. van Rheenen, M. W. Haakestad, IEEE Trans. THz Sci. Technol. 5, 3 (2015).
18. V. A. Trofimov, S. A. Varentsova, Sensors 15, 6 (2015).
19. U. Puc, A. Abina, M. Rutar, A. Zidansek, A. Jeglic, G. Valusis, Appl. Opt. 54, 14 (2015) .
20. W. Gao, Y. Jianquan, X. Degang, Adv. Mat. Res. (2013) doi:10.4028/www.scientific.net/AMR.760-762.492.
21. L. M. Zurk, B. Orlowski, D. P. Winebrenner, E. I. Thorsos, M. R. Leahy-Hoppa, L. M. Hayden, J. Opt. Soc. Am. B 24, 9 (2007).

22. E. M. Vartiainen, Y. Ino, R. Shimano, M. Kuwata-Gonokami, Y. P. Svirko, K. E. Peiponen, J. Appl. Phys. 96, 4171 (2004).
23. J. Zhao, W. Chu, L. Guo, Z. Wang, J. Yang, W. Liu, Y. Cheng, Z. Xu, Sci. Rep. (2014) doi:10.1038/srep03880.
24. M. Naftaly, R. Dudley, Opt. Lett. 34, 8 (2009).
25. D. Polder, J.H. van Santen, Phys. 12(5), 257-271 (1946).
26. C. Jördens, M. Scheller, S. Wietzke, D. Romeike, C. Jansen, T. Zentagraf, K. Wiesauer, V. Reisecker, M. Koch, Compos. Sci. Technol. 70(3), 472 (2010).
27. D. A. Newnham, P. F. Taday, Appl. Spectrosc. 62, 394 (2008).